

# **The CMIP6 historical simulations datasets produced by the climate system model CAMS-CSM**

Xinyao Rong<sup>1</sup>, Jian Li<sup>1</sup>, Haoming Chen<sup>1</sup>, Jingzhi Su<sup>1</sup>, Lijuan Hua<sup>1</sup>, Zhengqiu Zhang<sup>1</sup>, Yufei Xin<sup>1</sup>

<sup>1</sup> *State Key Laboratory of Severe Weather, Chinese Academy of Meteorological Sciences, Beijing 100081*

Corresponding author(s): Jian Li (lij@cma.gov.cn)

## Abstract

This paper describes the historical simulations produced by the Chinese Academy of Meteorological Sciences (CAMS) climate system model (CAMS-CSM), which are contributing for the sixth phase of the Coupled Model Intercomparison Project (CMIP6). The model description, experiment design and model outputs are presented. Three members' historical experiments are conducted by CAMS-CSM, with two members starting from different initial conditions, and one excluding the stratosphere aerosol to identify the effect of volcano eruptions. The outputs of the historical experiments are also validated using observational data. It is found that the model can reproduce the climatological mean states of the major climate system quantities, including the surface air temperature, precipitation, and the equatorial thermocline. The long-term trend of air temperature and precipitation is also reasonably captured by CAMS-CSM. There are still some biases in the model needs further improvement. This paper can help the users to better understand the performance and the datasets of the CAMS-CSM model.

**Key words:** CMIP6, historical simulation, CAMS-CSM, climate system model, data description

<https://doi.org/10.1007/s00376-020-0171-y>

## 1. Introduction

The interactions between the atmosphere, ocean, land and cryosphere form and maintain the earth's climate and its variation. The climate system model (CSM), or earth system model (ESM), which includes the major climate system components such as the atmosphere, ocean, land surface, and sea ice, is a fundamental tool for understanding and predicting the climate variabilities and climate changes. Since 1995, the World Climate Research Programme's (WCRP) Working Group on Coupled Modelling (WGCM) has successfully organized five phases of Coupling Model Intercomparison Project (CMIP), which is now advanced to the sixth phase (CMIP6) (Eyring et al., 2016). The simulations and prediction results from the climate models of past CMIP phases have constituted important and solid scientific foundation for the Intergovernmental Panel on Climate Change (IPCC) Assessment Report.

CMIP is designed to better understand past, present, and future climate change from unforced natural variability or in response to radiative forcing changes through multi-model simulations (Eyring et al., 2016). The CMIP historical simulations is an indispensable part of the entry card for participating CMIP6. They start from arbitrary equilibrium conditions from the pre-industrial control experiment (piControl) and integrate with time-dependent observational forcing, including greenhouse gases (GHG) emission (for ESM) or concentrations (for CSM), land-use forcing, anthropogenic aerosols, stratospheric aerosols (volcanoes), solar forcing, and ozone concentrations and nitrogen deposition etc. Therefore, the historical simulations can serve as the benchmark of model performance as these simulations can be validated against the observational records. The change of global mean surface temperature from pre-industrial to present in the historical simulations, as well as their spatial characteristics, are critical metrics of the model performance, which directly determine the reliability of the future climate projection produced by the model. In

China, the development of global climate models began in the 1980s and great achievements have been made in the past 40 years, including the involvement in every CMIP activities (Zhou et al., 2020).

In recent years, a climate system model, known as CAMS-CSM, was developed at the Chinese Academy of Meteorological Sciences (Rong et al., 2018). The performance of the early version of CAMS-CSM has been fully evaluated, including the climatology and seasonal cycle (Rong et al., 2018), climate sensitivity (Chen et al., 2019), intraseasonal variability (Qi et al., 2019; Ren et al., 2019; Wang et al., 2019), ENSO and the teleconnections (Hua et al., 2019; Lu et al., 2019), annular modes (Nan et al., 2019), land heat and water (Zhang et al., 2018), and so on. Based on the evaluation, a couple of updates are made for CAMS-CSM to improve its simulation on cloud radiative forcing and radiation transfer process. This new version CAMS-CSM is then devoted to the formal CMIP6 simulations. At present, CAMS-CSM has completed all the entry card simulations of CMIP6, and the model outputs have been published onto the Earth System Grid Federation (ESGF) data server (<https://esgf-data.dkrz.de/search/cmip6-dkrz/>). The purpose of this paper is to describe the configuration of CMIP6 version of CAMS-CSM model and the design of its historical experiments, then provide a brief validation of the results of the historical experiments as well as a comparison between the CMIP6 version and the previous version. Follow Guo et al. (2020), we will mainly validate the climatology of surface temperature, precipitation, as well as their long-term trends. As these metrics are fundamental for the evaluation of the historical simulations of climate models, some comparison between CAMS-CSM and FGOALS-f3-L model will be performed. In addition, we will also evaluate the ocean temperature, sea ice concentration, and interannual variability produced by this model, focusing mainly on the El Niño-Southern Oscillation (ENSO) phenomenon.

This paper is arranged as follows. Section 2 presents a brief introduction of the CMIP6 version of CAMS-CSM model and the design of its historical experiments. Section 3 describes the technical detail of the model output datasets. Section 4 presents some basic validation of the outputs from the historical simulations. Finally, a usage notes is provided in section 5.

## **2. Model and Experiments**

### ***2.1 Model***

The configuration of CAMS-CSM model used for CMIP6 simulations is described detailly in the paper by Rong et al. (2018). To facilitate the users of CAMS-CSM historical simulations datasets, here we provide again an introduction of the model.

The atmospheric component of CAMS-CSM model is a modified version of ECHAM5(v5.4) (Roeckner et al., 2003). The resolution adopted for CMIP6 historical simulations is T106 L31, which indicates a resolution of approximately  $1^\circ$  horizontally with 31 vertical levels. The top of the atmospheric model is 10 hPa. The major modifications of the CAMS-CSM version to the original ECHAM5 model include: i) a Two-step Shape Preserving Advection Scheme (TSPAS) for the water vapor advection (Yu, 1994; Zhang et al., 2013); and ii) a correlated k-distribution scheme with the Monte Carlo Independent Column Approximations (McICA) developed by Zhang et al. (2003, 2006a, 2006b) for radiation transfer calculation. There are two differences between the CMIP6 version and the early version used in Rong et al. (2018): i) a modification of the conversion rate from cloud water to precipitation in the cumulus convection scheme (from  $2 \times 10^{-4} \text{ m}^{-1}$  to  $1 \times 10^{-4} \text{ m}^{-1}$ ), which is able to improve the cloud radiative forcing simulation (Zhang et al., 2020); ii) and an effective solar zenith angle scheme accounting for the curvature of the atmosphere

and its effect on the length of the optical path of the direct solar beam with respect to a plane parallel atmosphere.

The ocean component is the Geophysical Fluid Dynamics Laboratory (GFDL) Modular Ocean Model version 4 (MOM4) (Griffies et al., 2004). The horizontal resolution is fixed to  $1^\circ$  zonally, with a variable meridional resolution:  $1/3^\circ$  within the  $10^\circ\text{S}$ – $10^\circ\text{N}$  and increases to  $1^\circ$  at  $30^\circ\text{S}$  (N), and a nominal  $1^\circ$  in the bipolar Arctic region poleward of  $60^\circ\text{N}$  for the tripolar grid. MOM4 employs a  $Z$  vertical coordinate that contains 50 vertical levels, with 23 even levels placed above 230 m to better represent the thermocline. The subgrid physical parameterization configured for the historical simulations is same as Rong et al. (2018), which includes: anisotropic Laplacian scheme for horizontal viscosity; isoneutral diffusion for tracer; K-Profile Parameterization (KPP) together with Bryan-Lewis vertical diffusion/viscosity schemes; tidal mixing, overflow for dense water crossing steep bottom topography; full convective adjustment scheme; and solar penetration with climatological chlorophyll concentration etc.

The sea ice component is the GFDL Sea Ice Simulator (SIS) (Winton, 2000), using the same grid as the ocean model. SIS is a thermodynamic/dynamic sea ice model. It adopts a three-layer structure: one snow layer and two sea ice layers of equal thick. In each grid there are five categories of sea ice and one open water area. Different categories' sea ice is redistributed based on an enthalpy conserving approach. The elastic–viscous–plastic technique developed by Hunke and Dukowicz (1997) is employed for the internal ice stresses calculations.

The Common Land Model (CoLM) (Dai et al., 2003) is utilized as the land component, using the same grid as the atmospheric model. In CoLM each surface grid cell is comprised of up to 24 land cover types. The soil is divided exponentially into 10 unequal vertical layers, with a thick of 1.75cm for the top layer and 114cm for the bottom layer, A two-big-leaf submodel is employed in

CoLM for photosynthesis, stomatal conductance, leaf temperature, and energy fluxes (Dai et al., 2004). The CAMS-CSM version implemented an unfrozen water process (Niu and Yang, 2006) that allows liquid water remains in the soil when temperature is below 0°C.

CAMS-CSM uses the GFDL Flexible Modelling System (FMS) coupler for fluxes/states calculations and interpolations among component models. For stability and efficiency considerations, a new conservative coupling algorithm is developed to guarantees the implicit treatment of the air-ice fluxes as well as a low communication cost among component models (Rong et al., 2018).

## ***2.2 Experiments designs***

We conducted three historical simulation experiments for CAMS-CSM (Table 1). The first experiment “r1i1p1f1” starts from the initial conditions of 1st January 3025 of the piControl experiment. The external forcing used for this simulation is from the recommendation of CMIP6 (<https://esgf-node.llnl.gov/projects/input4mips>), which includes historical greenhouse gases concentrations (CO<sub>2</sub>, CH<sub>4</sub>, N<sub>2</sub>O, CFC-12, and equivalent CFC-11 which accounting for the radiative effects of all 39 other gases) (Meinshausen et al., 2017), ozone concentrations (<http://blogs.reading.ac.uk/ccmi/forcing-databases-in-support-of-cmip6/>), stratospheric aerosols ([ftp://iacftp.ethz.ch/pub\\_read/luo/CMIP6/data\\_description.txt](ftp://iacftp.ethz.ch/pub_read/luo/CMIP6/data_description.txt)), the total solar irradiance (<http://solarisheppa.geomar.de/cmip6>), as well as the anthropogenic aerosols using simple plumes parameterization (Bjorn et al. 2016). Fixed land-use forcing is used in this simulation. The second simulation, “r2i1p1f1”, is same as “r1i1p1f1” but starts from a different date of piControl (i.e., 1st Jan 3030). To identify the effect of volcano eruptions, a third simulation “r1i1p1f2” is conducted, which is same as “r1i1p1f1” but excluded the historical stratospheric aerosols forcing. As required by CMIP6, all experiments were integrated from 1850 to 2014.

### 3. Data record

The datasets of the CMIP6 historical experiments for CAMS-CSM have been published onto the ESGF data server and can be accessed via searching the model name together with the experiment name (i.e., “historical”) at <https://esgf-data.dkrz.de/search/cmip6-dkrz/> or <https://esgf-node.llnl.gov/projects/cmip6/>. The data format is the Network Common Data Form (NetCDF), version 4, which can be read and visualized by scientific data analysis and visualization software like the NCAR Command Language (NCL, <http://www.ncl.ucar.edu>) or Python (<https://www.python.org>). Users can also process the data by command-line toolkits such as the Climate Data Operator (CDO, <https://code.mpimet.mpg.de/projects/cdo/>) or the NetCDF Operator (NCO, <http://nco.sourceforge.net>).

Monthly mean and daily mean outputs are provided for the CAMS-CSM datasets. There are 38 monthly mean variables for the atmospheric model dataset, including air temperature, humidity, velocity, sea level pressure, precipitation, radiation fluxes, surface heat fluxes and momentum fluxes, cloud water and cloud ice, cloud cover, etc. Totally 11 monthly mean variables of the oceanic model are provided, including sea temperature, salinity, velocity, surface heat flux, mixed layer depth, sea surface height etc. The monthly mean outputs of the land model contain 10 variables, including soil temperature, soil moisture and ice, evaporation, etc. The sea ice model provides 18 monthly mean variables, including sea ice concentration, temperature, velocity, thickness, sea ice transport, surface stress, surface snow thickness, etc. The daily mean outputs are provided only for atmospheric model, which contain 15 variables including air temperature, velocity, humidity, surface temperature, precipitation, radiative fluxes, etc.

### 4. Validation

The datasets used in this study for validation consist of the surface air temperature of the Japanese 55-year Reanalysis (JRA-55) (Kobayashi and Iwasaki, 2016), the land surface temperature data are from the Climatic Research Unit Temperature version 4 (CRUTEM4) (Osborn and Jones, 2014), sea ice concentration from HadISST (Rayner et al., 2003), the precipitation data of the Global Precipitation Climatology Project (GPCP), version 2.3 (Adler et al., 2003), Levitus94 ocean temperature data (Levitus and Boyer, 1994), the collaborative surface temperature data HadCRUT4 of the Met Office Hadley Center and the Climatic Research Unit at the University of East Anglia (Morice et al., 2012). The horizontal grids of JRA-55 data, GPCP data and HadCRUT4 data are  $288 \times 145$ ,  $144 \times 72$  and  $72 \times 36$ , respectively. The JRA-55 data and GPCP data are interpolated to the CAMS-CSM grid for comparison.

#### ***4.1 Climatology of temperature, precipitation and sea ice***

Here we first examine two fundamental metrics for coupled climate model performance: climatological annual mean surface air temperature and precipitation. Figure 1 shows the simulated and observed surface air temperature climatology. It can be seen that the model reasonably reproduces the global distribution of surface air temperature. The overall spatial pattern of the simulated surface air temperature resembles that from the observations. Over much of the ocean and terrestrial areas the biases are less than  $1^\circ\text{C}$  (the global averaged biases is  $-0.145^\circ\text{C}$ , and the root mean square error (RMSE) is  $2.42^\circ\text{C}$ ). Evident biases primarily lie in the North Atlantic and the Southern Ocean near Antarctic, where the biases can be larger than  $5^\circ\text{C}$  (with a significant level of 5%). The cold biases over the high latitudes of North Atlantic is associated with the overestimated sea ice cover in the northern hemisphere, while the warm biases near Antarctic might be ascribed to the underestimated sea ice extent over there (Fig. 4). In the eastern coastal regions of the tropical Pacific and Atlantic, the simulated surface temperature tends to be warmer

than the observation, which can be usually seen in coupled climate models and may result from the inadequate representation of stratocumulus and coastal upwelling in coupled models. We also calculated the surface air temperature error over land using CRUTEM4 data. The result shows that the global mean biases and RMSE over land are  $-0.128^{\circ}\text{C}$  and  $2.14^{\circ}\text{C}$ , smaller than those of previous version are  $-1.53^{\circ}\text{C}$  and  $2.31^{\circ}\text{C}$ , suggesting a performance improvement of the CMIP6 version.

Figure 2 shows the simulated and observed annual mean precipitation. Overall, the simulated precipitation shows a similar pattern with the observations (the global averaged biases  $0.03\text{ mm day}^{-1}$ , and the RMSE is  $1.15\text{ mm day}^{-1}$ ). The active precipitation centers, such as the intertropical convergence zone (ITCZ), south Pacific convergence zone (SPCZ), the south Atlantic convergence zone (SACZ), as well as those over the tropical Indian ocean and subtropical oceans, are reasonably captured by the model. Compared with the GPCP data, the simulated precipitation in the tropical oceans are generally overestimated, especially over the areas of ITCZ and SPCZ, where the biases can exceed  $4\text{ mm day}^{-1}$  and the general precipitation pattern in the tropical Pacific tends to bear a double-ITCZ structure. To some extent, the double-ITCZ bias is improved compared with the previous version (Rong et al. 2018), however, it still remains a prominent discrepancy of the CAMS-CSM model. Though it is recognized that the double-ITCZ errors arise from the Bjerknes feedback between atmosphere and ocean, how to eliminate this bias remains unresolved and the double-ITCZ still stands out as a prevailing error in current coupled models (Zhang et al. 2015). It is worthy to mention that the double-ITCZ bias is largely reduced in the FGOALS-f3-L model (Guo et al., 2020), which might benefit from the convection scheme adopted in the model, suggesting that improvement of physical schemes might be an effective way to eliminate the double-ITCZ error. Over the tropical Atlantic, the simulated SACZ shifts southward

to the warm SST biases area, with excessive precipitation in the tropical south Atlantic. Dry biases can be found in the central and eastern equatorial Pacific, as a result of an overestimated cold tongue in the model. There exists certain connection between the temperature biases and precipitation biases over some land areas. For example, the warm biases over tropical Africa and Amazon appear to be associated with the dryer biases over these regions, while the cold biases in the Tibetan Plateau corresponds to an overestimated precipitation.

The equatorial thermocline plays crucial role in the climate variability of the tropical Pacific. Fluctuation of thermocline depth is tightly connected with the sea surface temperature anomalies associated with the El Niño-Southern Oscillation (ENSO) phenomenon. Figure 3 shows the simulated annual mean upper ocean temperature along the equatorial oceans. Here we use the depth of 20°C isotherm to represent the thermocline depth. It can be seen that the west-east tilted feature of equatorial Pacific thermocline is well depicted by the model. In the equatorial Pacific, the 20°C isotherm of the model generally follows that of the observation. The discrepancy is that the simulated thermocline exhibits a kind of weaker zonal slope compared with the observation, which is primarily manifested by a slightly shallower thermocline of the model in the western Pacific. The 20°C isotherms in the Indian Ocean and Atlantic Ocean are also reasonably reproduced, with a weaker relative to the observation. Below 150m of the Pacific Ocean, the isotherms generally follow the observation, while warm biases can be found over the Indian and Atlantic oceans.

Figure 4 shows the climatologically mean sea ice concentration for the historical simulations. The line (thick cyan) of 15% mean concentration from the HadISST data is presented for comparison. In general, the model is able to depict the seasonal evolution of sea ice concentrations. During FMA, the simulated Arctic sea ice extends too much to the equator, in particular over the

North Atlantic Ocean, whereas during ASO the sea ice cover is in agreement with the observation. Analogous to the previous version (Rong et al., 2018), the Antarctic sea ice is underestimated by the model, especially during FMA, the sea ice is visible over some areas of the Ross Sea and Weddell Sea. The excessive /insufficient sea ice cover concentrations in Arctic/Antarctic leads to the warm/cold biases in the surface temperature over these regions, indicating that the sea ice need further improvement to enhance the temperature simulation.

#### ***4.2 Interannual variability***

Figure 5a and 5b show the standard deviation of the Niño3.4 index from the observations and model. It can be seen that the amplitude of the simulated Niño3.4 SST variability is consistent well with the HadISST data. Similar to the observation, the simulated ENSO tend to mature during the winter, indicating a reasonable phase locking feature produced by the model. In particular, the overestimated ENSO amplitude in the previous version of CAMS-CSM is remarkably reduced, which may be ascribed the improvement in convection and cloud radiative forcing over the tropical Pacific due to the modification of cumulus scheme. Note that in current version there is a secondary peak occurring near May, which is not observed in previous version. The spatial distribution of simulated SST variability also shows a reasonable pattern with respect to the observation (Fig. 5a,b), with the maximum center locates on the central-eastern equatorial Pacific. Compared with the observation, the SST variance is underestimated over the coastal region of the South America, which is a common bias in coast resolution coupled models and is ascribed to the insufficient coastal upwelling in these models.

#### ***4.3 Long-term trend***

As mentioned above, the change of global mean surface temperature from pre-industrial to present in historical simulations is a key metric of the model performance. Figure 6a shows the

simulated and observed global mean surface air temperature anomalies from 1850 to 2014. It can be seen that all three ensemble members can reasonably capture the long-term warming trend since 1850, as well as the rapid warming after 1980. As three ensemble members starts from different initial conditions or using different forcing, the transient phases among them are inconsistent except during the major volcano eruption periods. For example, the global mean surface air temperature of “r1i1p1f1” and “r2i1p1f1” shows notable decline near the eruption periods of volcano Krakatoa (1883), volcano Mount Pelée (1902) and volcano Pinatubo (1991), while in “r1i1p1f2” such a global cooling is absent because the stratosphere aerosols are excluded in this simulation. Compared with the observations, the simulated cooling in responses to volcano eruption is overestimated, especially during volcano Pinatubo, leading to a weaker warming in both “r1i1p1f1” and “r2i1p1f1” experiments after 1990s. The simulation of “r1i1p1f2”, however, shows a comparable warming trend as the observation. The averaged least-squares linear trends of the three simulations from 1850-2014 are 0.041(r1i1p1f1), 0.040(r2i1p1f1), 0.046 (r1i1p1f2) °C (10 yr)<sup>-1</sup>, slightly weaker than that of the observation (0.048°C (10 yr)<sup>-1</sup>). Note that the warming of “r1i1p1f2” after 1980 is remarkably stronger than “r1i1p1f1” and “r2i1p1f1”. The linear trends of HadCRUT4 data, “r1i1p1f1”, “r1i1p1f2” and “r1i1p1f2” from 1980-2014 are 0.161, 0.137, 0.138 and 0.204 °C (10 yr)<sup>-1</sup>, respectively, suggesting a robust cooling effect of volcano Pinatubo in this model. It can be seen that the warming trend produced in the CAMS-CSM is weaker than that of the FGOALS-f3-L model, in which the trend tends to be greater than the observation, suggesting different climate sensitivities of two models. The observed precipitation time series exhibits a slightly wetting trend after 1980s, which is captured by three ensemble members’ simulations of the model. Before 1980s, the simulated precipitation shows significant interannual fluctuation without obvious long-term trend.

Figure 7 shows the linear trend of the simulated and observed zonal mean air temperature from 1960 to 2014. In general, the model well captures the major pattern of the trend in air temperature from surface to 10hPa. The observed trend of air temperature mainly shows a reversed distribution between the troposphere (below 150 hPa) and stratosphere (above 150 hPa), reflecting a typical structure of air temperature changes in response to increasing greenhouse gases (Fig. 7b). Over the polar region of southern hemisphere, the observed trend exhibits a sandwich structure, i.e., warming trend below 300 hPa and above 30 hPa, and a cooling trend between 300 hPa and 30 hPa. The model is able to reproduce the contrary trend between troposphere and stratosphere, and the simulated magnitude of the trend is comparable with that of the observation. Noting that the complex structure over the southern polar region is successfully captured by the model, especially the warming center above 30 hPa, which seems absent in the FGOALS-f3-L model (Guo et al., 2020). There is some deficiency, however, exists in the model. For example, the maximum cooling in the model shift toward to the lower stratosphere, and the warming trend in the lower troposphere over the southern and northern polar regions is somewhat underestimated.

## 5. Usage Notes

As the top of the atmospheric model is 10 hPa, the values above 10 hPa are unrealistic and have been filled with missing values in the atmospheric pressure level datasets.

The ocean component (MOM4) and sea ice component (SIS) of CAMS-CSM use a tripolar grid, which is comprised of a bipolar Arctic grid (two northern poles are placed over the North American and Eurasian land areas) and a normal spherical latitude–longitude grid. As tripolar grid model uses generalized orthogonal curvilinear coordinates, its  $X$  and  $Y$  directions are orthogonal over the bipolar region, but no longer parallel to latitude–longitude circles. Instead, there are geographically

varying angles between two grids. At present, the oceanic and sea ice output dataset of CAMS-CSM published on ESGF node are on the original tripolar grid (i.e., grid label “gn”, means the model’s native grid), thus specific consideration is required before visualization the datasets. For scalar variables, users can directly analyze and visualize the dataset by software that support curvilinear grids (i.e., grids represented by two-dimensional latitude/longitude arrays) such as NCL or Python. An alternative choice is to interpolate the original data to a latitude–longitude grid using CDO or NCO, which can be easily processed by command-line operations. For vector variables over the latitude-longitude grid area (southward of 60°N), users can directly analyze or visualize the data using normal scientific data analysis and visualization software. While over the bipolar Arctic region poleward of 60°N, rotations are needed before visualization or interpolation, which should be performed in terms of the angles between the original orthogonal curvilinear grid and the latitude–longitude grid.

### **Acknowledgments**

This work was supported by the National Key Research and Development Program of China (No. 2019YFC1510001), the National Natural Science Foundation of China (No. 91637210), the Basic Research Fund of CAMS (No. 2018Z007) and the Jiangsu Collaborative Innovation Center for Climate Change.

### **Data availability statement**

The data that support the findings of this study are available from the following open sources: <https://esgf-data.dkrz.de/search/cmip6-dkrz/> or <https://esgf-node.llnl.gov/projects/cmip6/>. The citation of the historical simulations is “CAMS CAMS\_CSM1.0 model output prepared for CMIP6

CMIP historical. Version 20190708. Earth System Grid Federation.  
<https://doi.org/10.22033/ESGF/CMIP6.9754>”.

### **Disclosure statement**

No potential conflicts of interest are reported by the authors.

### **References**

Adler, R., and Coauthors, 2003: The version-2 global precipitation climatology Project (GPCP) Monthly precipitation analysis (1979–Present). *Journal of Hydrometeorology*, 4, 1147–1167, [https://doi.org/10.1175/1525-7541\(2003\)004<1147:TVGPCP>2.0.CO;2](https://doi.org/10.1175/1525-7541(2003)004<1147:TVGPCP>2.0.CO;2).

Bjorn, Steven, Stephanie, et al., 2016: Simple Plumes: A parameterization of anthropogenic aerosol optical properties and an associated effect for climate studies. *Geoscientific Model Development Discussions*, <https://doi.org/10.5194/gmd-2016-189>

Chen, X. L., Guo Z., Zhou T. J., et al., 2019: Climate sensitivity and feedbacks of a new coupled model CAMS-CSM to idealized CO<sub>2</sub> forcing: A comparison with CMIP5 models. *J. Meteor. Res.*, 33, 31-45., <https://doi.org/10.1007/s13351-019-8074-5>

Dai Y., X. Zeng, R. E. Dickinson, I. Baker, G. B. Bonan, M. G. Bosilovich, A. S. Denning, P. A. Dirmeyer, P. R. Houser, G. Niu, K. W. Oleson, C. A. Schlosser, and Z. L. Yang, 2003: The common land model. *Bull. Amer. Meteor. Soc.*, 84, 1013–1023, doi:10=1175=BAMS-84-8-1013.

Dai, Y., R. E. Dickinson, and Y. P. Wang, 2004: A two-big-leaf model for canopy temperature, photosynthesis, and stomatal conductance. *J. Climate*, 17, 2281–2299, doi:10.1175/1520-0442(2004)017<2281:ATMFCT>2.0.CO;2.

Eyring, V., S. Bony, G. A. Meehl, et al., 2016: Overview of the Coupled Model Intercomparison Project Phase 6 (CMIP6) experimental design and organization. *Geoscientific Model Development*, 9, 1937–1958, doi:10.5194/gmdd-8-10539-2015.

Griffies, S. M., M. J. Harrison, P. C. Pacanowski, et al., 2004: A Technical Guide to MOM4. GFDL Ocean Group Technical Report NO. 5, 339 pp.

Guo, Y., Y. Q. Yu, P. F. Lin, H. L. Liu, B. He, Q. Bao, S. Zhao, and X. Wang, 2020: Overview of the CMIP6 historical experiment datasets with the climate system model CAS FGOALS-f3-L. *Adv. Atmos. Sci.*, <https://doi.org/10.1007/s00376-020-2004-4>.

Hua, L. J., Chen L., Rong X. Y., et al., 2019: An assessment of ENSO stability in CAMS climate system model simulations. *J. Meteor. Res.*, 33, 80–88, <https://doi.org/10.1007/s13351-018-8092-8>

Kobayashi, C., and T. Iwasaki, 2016: Brewer-dobson circulation diagnosed from JRA-55. *J. Geophys. Res.*, 121, 1493–1510, <https://doi.org/10.1002/2015JD023476>.

Levitus, S., Boyer T.P., 1994: World Ocean Atlas 1994 Volume 4: Temperature, number 4.

Lu, B., Ren H. L., 2019: ENSO features, dynamics, and teleconnections to East Asian climate as simulated in CAMS-CSM. *J. Meteor. Res.*, 33, 46–65, <https://doi.org/10.1007/s13351-019-8101-6>

Meinshausen, M., Vogel, E., Nauels, A., Lorbacher, K., Meinshausen, N., Etheridge, D. M., ... & Krummel, P. B. (2017). Historical greenhouse gas concentrations for climate modelling (CMIP6). *Geoscientific Model Development*, 10, 2057–2116.

Morice, C. P., J. J. Kennedy, N. A. Rayner, and P. D. Jones, 2012: Quantifying uncertainties in global and regional temperature change using an ensemble of observational estimates: The HadCRUT4 data set. *J. Geophys. Res.*, 117, D08101, <https://doi.org/10.1029/2011JD017187>.

Nan, S., Yang J., Bao Y., et al., 2019: Simulation of the Northern and Southern Hemisphere Annular Modes by CAMS-CSM. *J. Meteor. Res.*, 33, 949-959, <https://doi.org/10.1007/s13351-019-8099-9>

Niu, G. Y., and Z. L. Yang, 2006: Effects of frozen soil on snowmelt runoff and soil water storage at a continental scale. *J. Hydrometeorology*, 7, 937–952, doi:10.1175/JHM538.1.

Osborn, T.J. and P.D. Jones, 2014: The CRUTEM4 land-surface air temperature data set: construction, previous versions and dissemination via Google Earth. *Earth Syst. Sci. Data.*, 6, 61-68, doi:10.5194/essd-6-61-2014.

Qi, Y. J., Zhang R. H., Rong X. Y., et al., 2019: Boreal summer intraseasonal oscillation in the Asian–Pacific monsoon region simulated in CAMS-CSM. *J. Meteor Res*, 2019, 33, 66-79, <https://doi.org/10.1007/s13351-019-8080-7>

Rayner, N. A., D. E. Parker, E. B. Horton, C. K. Folland, L. V. Alexander, D. P. Rowell, E. C. Kent, and A. Kaplan, 2003: Global analyses of sea surface temperature, sea ice, and night marine

air temperature since the late nineteenth century. *J. Geophys. Res.*, 108, 1063-1082, doi:10.1029/2002JD002670.

Ren, P., Li G., Ren. H. L., et al., 2019: Representation of the Madden–Julian Oscillation in CAMS-CSM. *J. Meteor. Res.*, 33, 627-650, <https://doi.org/10.1007/s13351-019-8118-x>

Roeckner, E., and Coauthors, 2003: The atmospheric general circulation model ECHAM5. Part I: Model description. Rep. No.349, Max-Planck-Institut für Meteorologie, Hamburg, Germany, 127 pp.

Rong X. Y., Li J, Chen H M, et al.,2018: The CAMS climate system model and a basic evaluation of its climatology and climate variability simulation. *Journal of Meteorological Research*, 32 (6): 839-861. <https://doi.org/10.1007/s13351-018-8058-x>

Wang, L., Zhou T., Li J., et al., 2019: Convectively Coupled Equatorial Waves Simulated by CAMS-CSM Model. *J. Meteor. Res.*, 33, 666-677, <https://doi.org/10.1007/s13351-019-9021-1>

Wei, T., Li J., Rong X. Y., et al., 2018: Arctic climate changes based on historical simulations (1900–2013) with the CAMS-CSM. *J. Meteor. Res.*, 32, 881-895, <https://doi.org/10.1007/s13351-018-7188-5>

Winton, M., 2000: A reformulated three-layer sea ice model. *J. Atmos. Oceanic Technol.*, 17, 525-531, doi:10.1175/1520-0426(2000)017<0525:ARTLSI>2.0.CO;2.

Yu, R., 1994: A two step shape preserving advection scheme. *Adv. Atmos. Sci.*, 11, 479–490, doi:10.1007/BF02658169.

Zhang, B., Guo Z., Chen X., Zhou T., Rong X., Li J., 2020: responses of cloud-radiative forcing to strong El Niño events over the western Pacific warm pool simulated by CAMS-CSM. *J. Meteor. Res.*, doi: 10.1007/s13351-020-9161-3

Zhang, G., Li J. D., Rong X. Y., et al., 2018: An assessment of CAMS-CSM in simulating land-atmosphere heat and water exchanges. *J. Meteor. Res.*, 32, 862-880, <https://doi.org/10.1007/s13351-018-8055-0>

Zhang, H., T. Nakajima, G.-Y. Shi, T. Suzuki, and R. Imasu, 2003: An optimal approach to overlapping bands with correlated  $k$ -distribution method and its application to radiative calculations. *J. Geophys. Res.* **108**(D20), 4641.

Zhang, H., G. Shi, T. Nakajima, et al. 2006a: The effects of the choice of the  $k$ -interval number on radiative calculations. *Journal of Quantitative Spectroscopy and Radiative Transfer*, **98**, 31-43, <https://doi.org/10.1016/j.jqsrt.2005.05.090>.

Zhang, H., T. Suzuki, T. Nakajima, et al., 2006b: Effects of band division on radiative calculations. *Optical Engineering*, **45**, 016002, <https://doi.org/10.1117/1.2160521>.

Zhang, X., H. Liu, and M. Zhang 2015: Double ITCZ in coupled ocean-atmosphere models: from CMIP3 to CMIP5. *Geophys. Res. Lett.*, 42, 8651–8659, doi:10.1002/2015GL065973.

Zhang, Y., R. Yu, J. Li, and H. Chen, 2013: An implementation of a leaping point Two-step Shape-Preserving Advection Scheme in the high resolution spherical latitude-longitude grid. *Acta. Meteorol. Sin.*, 71, 1089–1102, <https://doi.org/10.11676/qxxb2013.085>.

Data description article submitted to AAS Special Issue on CMIP6

Zhou, T. J., Z. M. Chen, L. W. Zou, et al., 2020: Development of Climate and Earth System Models in China: Past achievements and new CMIP6 results. *J. Meteor. Res.*, 34(1), 1–19, doi: 10.1007/s13351-020-9164-0.

*in press*

**Table 1.** Experiments design.

Experiment_id	Variant_label	Integration time	Experiment design
historical	r1i1p1f1	1850–2014	Starts from 1st January 3025 of the piControl experiment. The external forcing includes historical greenhouse gases (CO <sub>2</sub> , CH <sub>4</sub> , N <sub>2</sub> O, CFC-12, and equivalent CFC-11), ozone concentrations, stratospheric aerosols, the total solar irradiance and the anthropogenic aerosols. Land-use forcing is fixed in this simulation.
historical	r2i1p1f1	1850–2014	Same as r1i1p1f1, but starts from 1st January 3030 of the piControl experiment.
historical	r1i1p1f2	1850–2014	Same as r1i1p1f1, but excludes the stratosphere aerosol forcing.

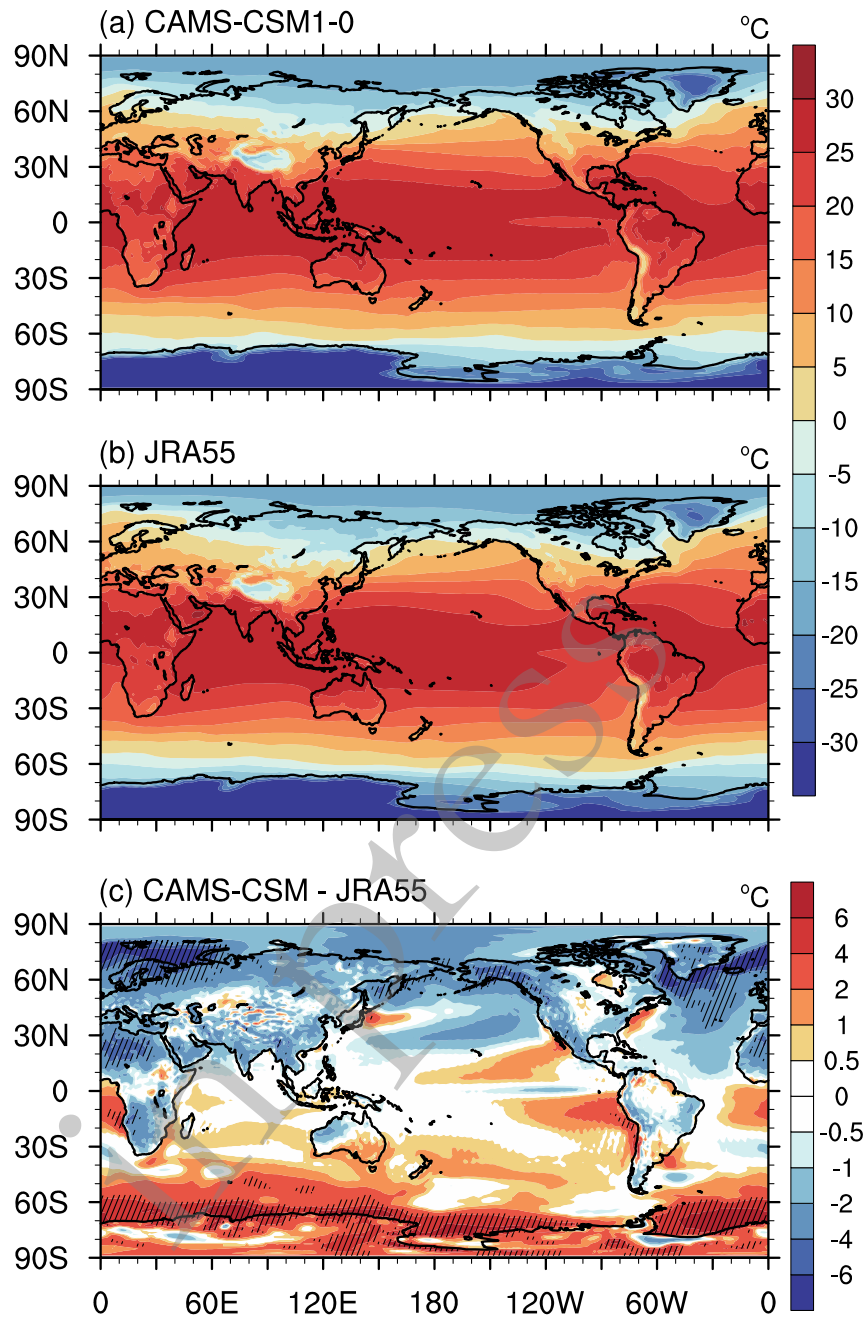


Figure 1 The climatology (1980-2014 averaged) of surface air temperature at 2m: (a) ensemble mean of CAMS-CSM historical simulations (r1i1p1f1 and r2i1p1f1); (b) JRA-55 data; (c) differences between CAMS-CSM historical simulations and JRA-55 data. The shadow areas in the plots denote the significant levels of 5% from the t-test against the interannual anomalies. Unit: °C.

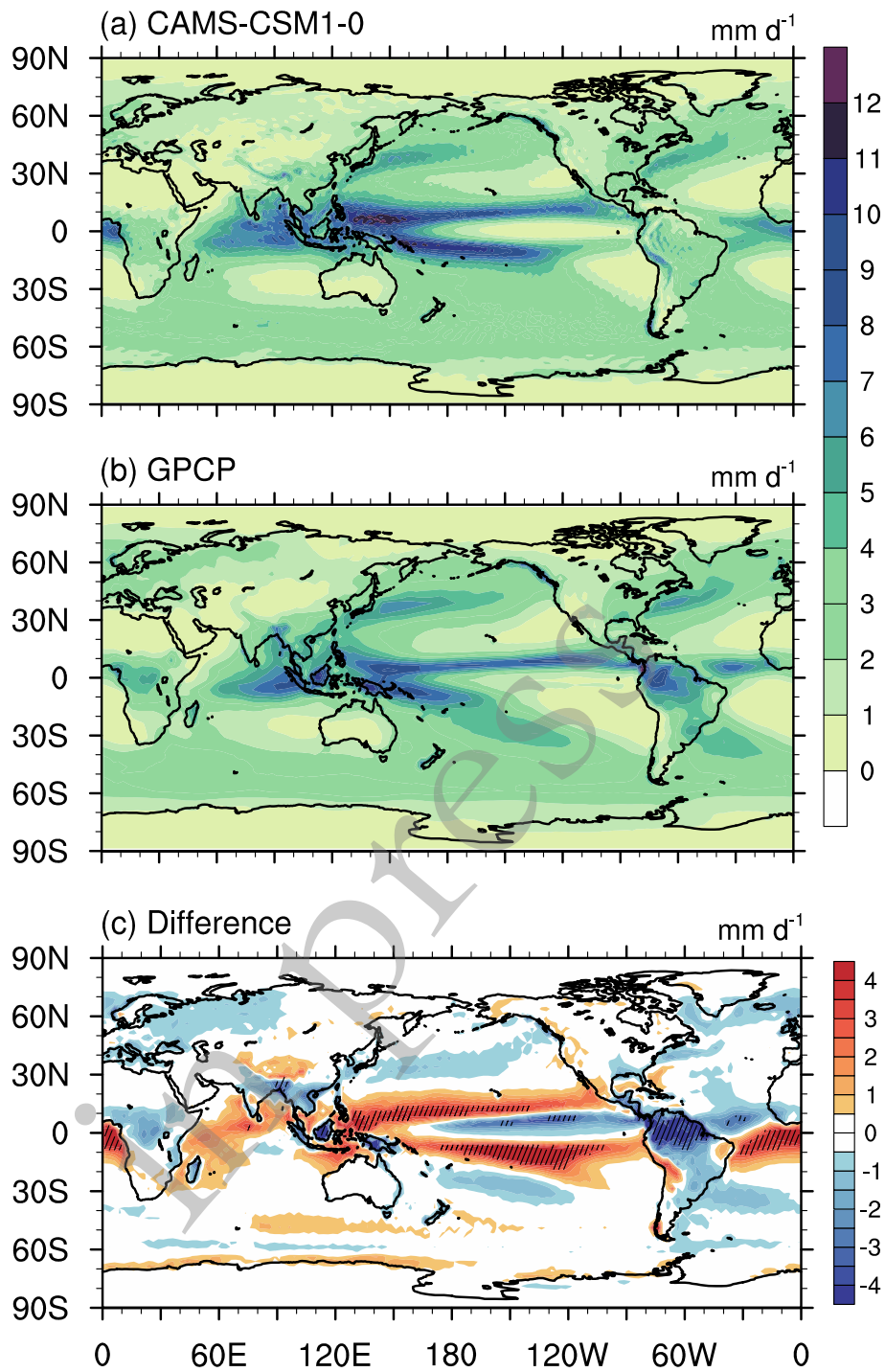


Figure 2 The climatology (1980-2014 averaged) of precipitation: (a) ensemble mean of CAMS-CSM historical simulations (r1i1p1f1 and r2i1p1f1); (b) GPCP data; (c) differences between CAMS-CSM historical simulations and GPCP data. The shadow areas in the plots denote the significant levels of 5% from the t-test against the interannual anomalies. Unit:  $\text{mm day}^{-1}$ .

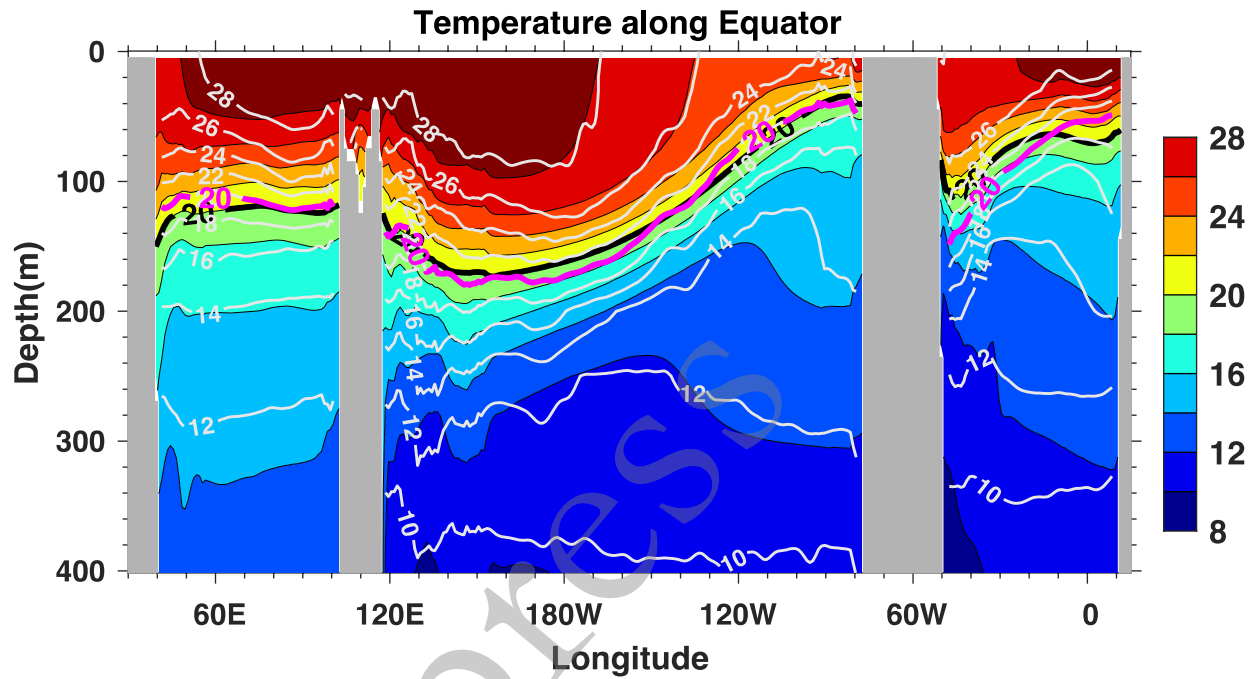


Figure 3 Annual mean temperatures ( $^{\circ}\text{C}$ ) along the equator ( $5^{\circ}\text{S}$ - $5^{\circ}\text{N}$ ) derived from the CAMS-CSM historical simulation (black contours-shading) and Levitus94 climatology (white contours). The black and red thick lines indicate the  $20^{\circ}\text{C}$  isotherm from CAMS-CSM and Levitus94 climatology, respectively. Unit:  $^{\circ}\text{C}$ .

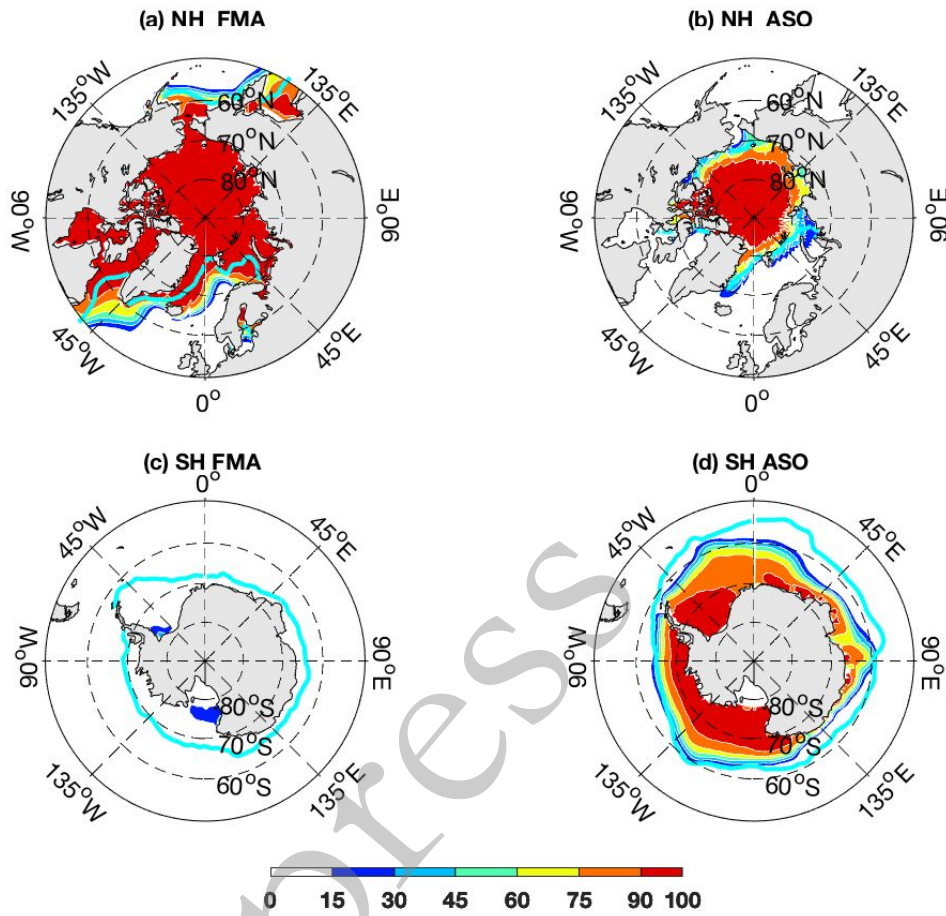


Figure 4 Climatological sea ice concentration in the Arctic (upper panels) and Antarctica (bottom panels) for the period of 1980-2014 for the historical simulations. The thick cyan lines indicate the 15% mean concentration values from the HadISST data with the same period. The left and right panels denote the averages for Feb.-Apr. and Aug.-Oct., respectively.

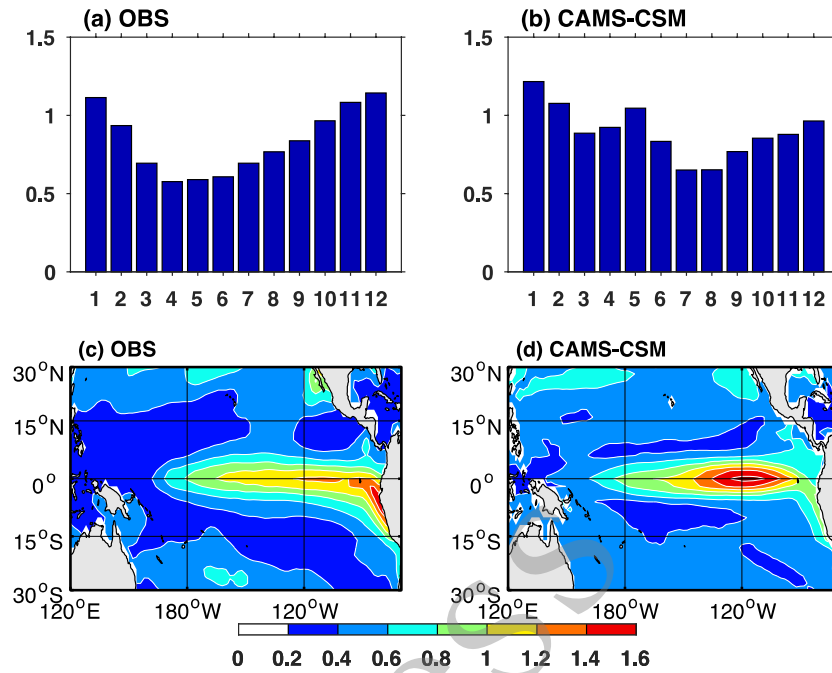


Fig. 5 Standard deviation of the Niño3.4 index (SSTA averaged over 170°E-120°E, 5°S-5°N) for each calendar month as derived from the (a) CAMS-CSM (red bar) and (b) HadISST data. (c) and (d) show the standard deviation of SST anomalies from the CAMS-CSM and HadISST data, respectively. Unit: °C.

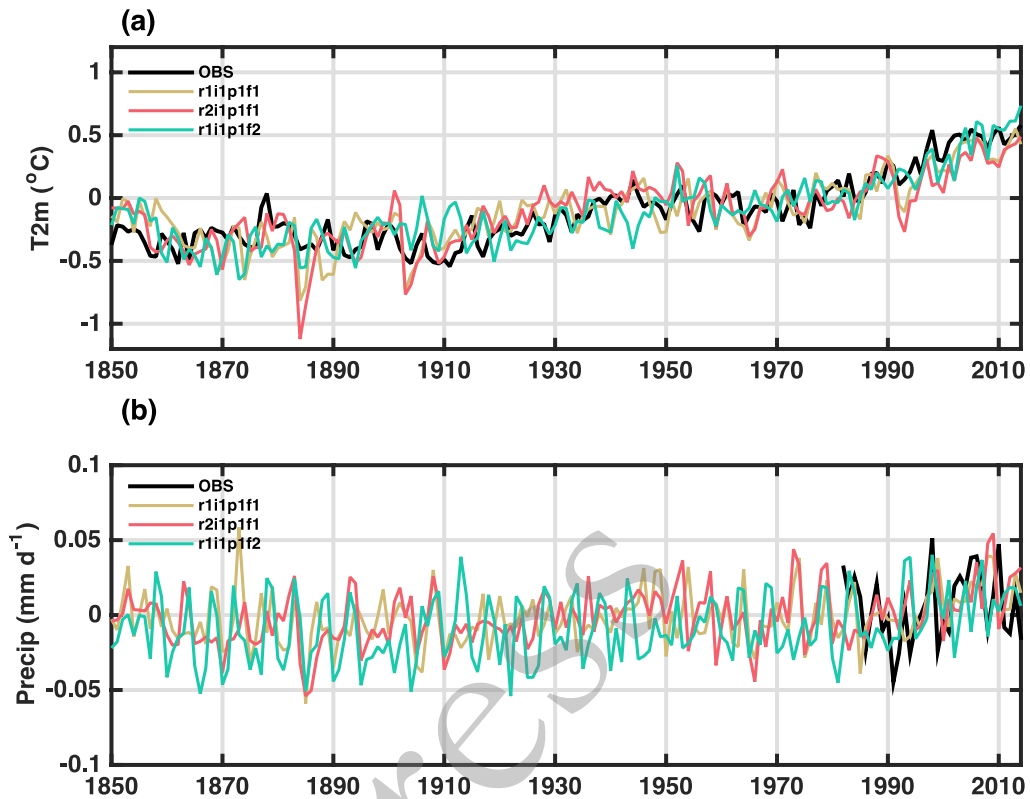


Figure 6 Global mean (a) surface air temperature ( $^{\circ}\text{C}$ ) and (b) precipitation ( $\text{mm day}^{-1}$ ) anomalies (annual mean) relative to the period 1961–1990 for CAMS-CSM historical experiments and observation. The observational data for surface air temperature and precipitation are HadCRUT4 and GPCP, respectively.

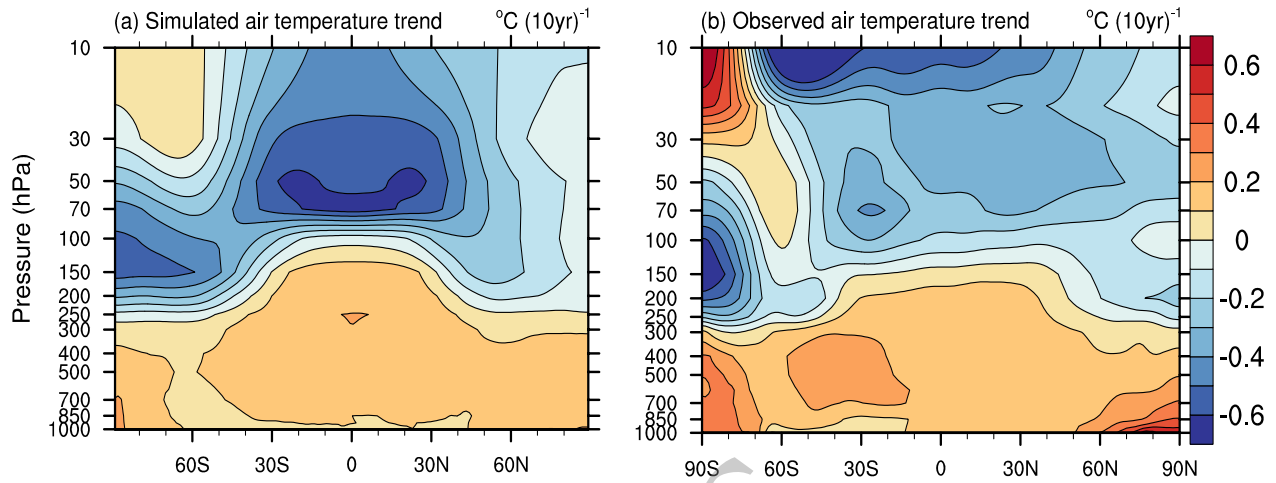


Figure 7 Linear trends of zonal mean air temperature from 1960 to 2014 for the (a) ensemble mean of CAMS-CSM historical experiments (r1i1p1f1 and r2i1p1f1) and (b) observation (JRA-55).